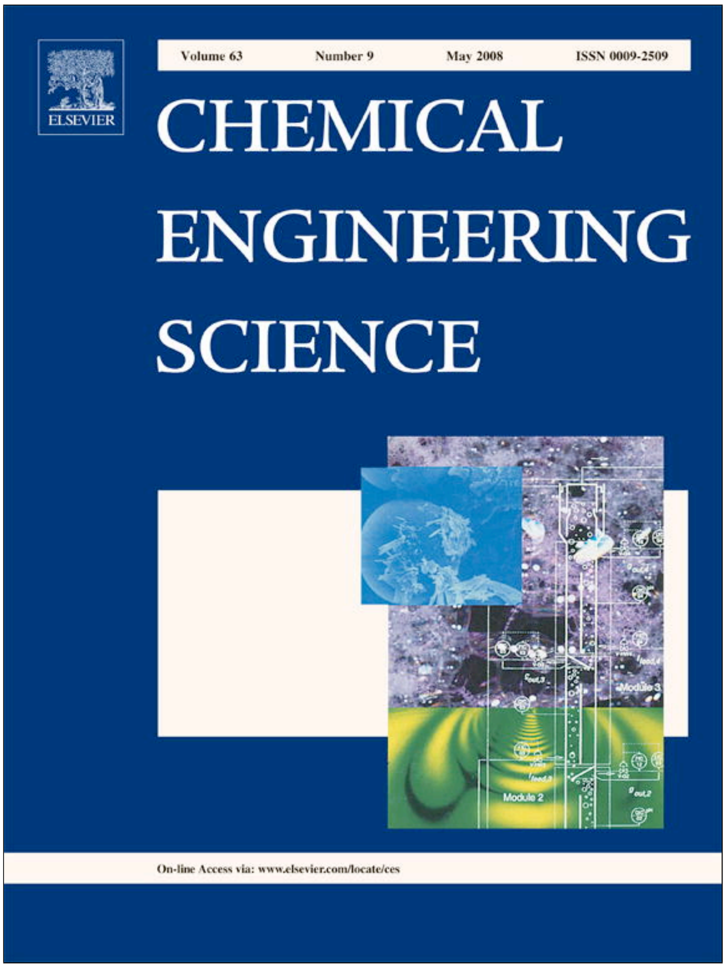
Volume 63
Number 9
May 2008
ISSN 0009-2509
ELSEVIER
CHEMICAL ENGINEERING SCIENCE
Module 3
Module 2
On-line Access via: www.elsevier.com/locate/ces

ELSEVIER

Chemical Engineering Science 63 (2008) 2548–2558

Chemical Engineering Science

www.elsevier.com/locate/ces

Fluctuations in dense phase pneumatic conveying of pulverised coal measured using electrical capacitance tomography

B.J. Azzopardi[a,*], K. Jackson[a], J.P. Robinson[a], R. Kaji[a], M. Byars[b], A. Hunt[b]

[a]School of Chemical and Environmental Engineering, University of Nottingham, University Park, Nottingham NG7 2RD, UK
[b]Tomoflow Ltd, 86 Water Lane, Wilmslow, Cheshire SK9 5BB, UK

Received 28 August 2007; received in revised form 1 February 2008; accepted 5 February 2008
Available online 14 February 2008

Abstract

A twin-plane electrical capacitance tomography (ECT) system has been employed to monitor the flow rate of fine coal transported by air in a 36.8 mm diameter pipe at mass fluxes of 1680 kg/m^2 s. The mean mass flow rate was obtained to be within $< 1\%$ of the value determined from load cells. The ECT output indicated that there were two types of systematic fluctuations in the time series of mass flow rate and concentration. The frequencies of these have been obtained from power spectral density analyses. For the higher frequency fluctuations, the Strouhal number (fD_t/u_{gs}) was found to depend on the square root of the solids/gas momentum flux ratio. An examination of the cross-sectional distribution of solids showed that the coal was concentrated around the wall of the pipe and that the concentration fluctuated as noted above.

Keywords: Gas/solids; Dense phase; Metering; Electrical capacitance; Tomography

1. Introduction

Pneumatic conveying of solids to feed reactors or purely to transport material has been studied for many years, e.g., Albright et al. (1951). This operation is carried out with wide ranges of gas velocities and solids flow rates. Particle sizes can also vary over a wide range, from 22 μm (Geldart and Ling, 1985) to several mm. Many studies have concentrated on the pressure gradient/solids flow rate/gas velocities relationships which are essential for design of conveying systems. Vertical, horizontal and inclined pipes are considered. Typical relationships, between the three parameters noted above, are sketched in Fig. 1. The region with a positive slope of pressure gradient/gas velocity is usually termed the dilute region. Decreasing the gas velocity leads to stronger, lower frequency fluctuations in pressure gradient and particle concentration as indicated by, e.g., Matsumoto and Harakawa (1987). In this region the solids can travel as plugs, the slug flow reported in some papers. However, it is not possible to know, by direct observation or by the use of optical transmitter/receiver method employed by Matsumoto and Harakawa (1987), what is occurring in the centre of the plug.

Three-dimensional and non-intrusive visualisation techniques will allow accurate correlations to be established and the many theoretical approaches in this area to be validated. Data from individual particles can be obtained by using positron emission particle tracking as applied by Van de Velden et al. (2007) to circulating fluidised beds. However, with this technique data have to be built up over time and only time-averaged information can be gathered. An alternative technique, electrical capacitance tomography (ECT), has been shown to be a useful tool in a number of fluidisation and pneumatic conveying studies. ECT uses a similar principle to the capacitance meter presented by Geldart and Ling (1985) which measured the capacitance between a pair of electrodes. However, in contrast to that earlier work, because ECT uses several pairs of electrodes mounted around the pipe circumference a high accuracy can be achieved. The capacitance is measured between each electrode pair, and the data used to develop a three-dimensional image of the solids volume fraction across the entire cross-section. With two electrode sets placed a short distance apart the data can be

* Corresponding author. Tel.: +44 115 951 4167; fax: +44 115 951 4181.
E-mail address: barry.azzopardi@nottingham.ac.uk (B.J. Azzopardi).

0009-2509/$ - see front matter © 2008 Elsevier Ltd. All rights reserved.
doi:10.1016/j.ces.2008.02.013

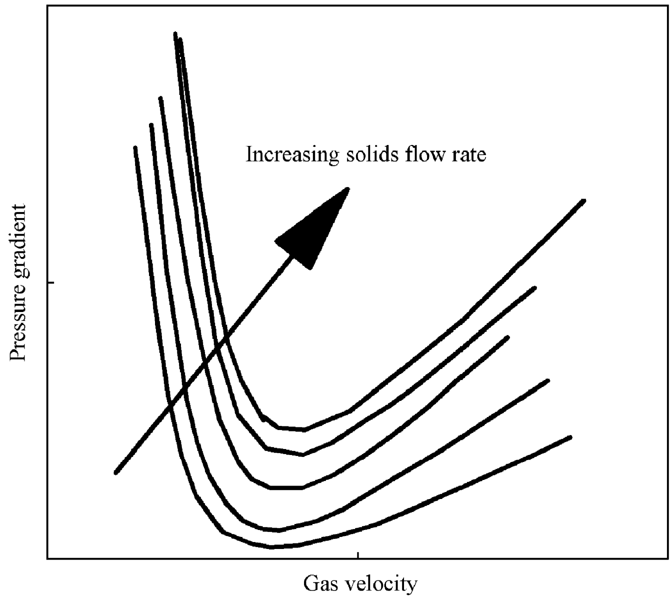

Fig. 1. Sketch of relationship between pressure gradient gas velocity and solids flow rate.

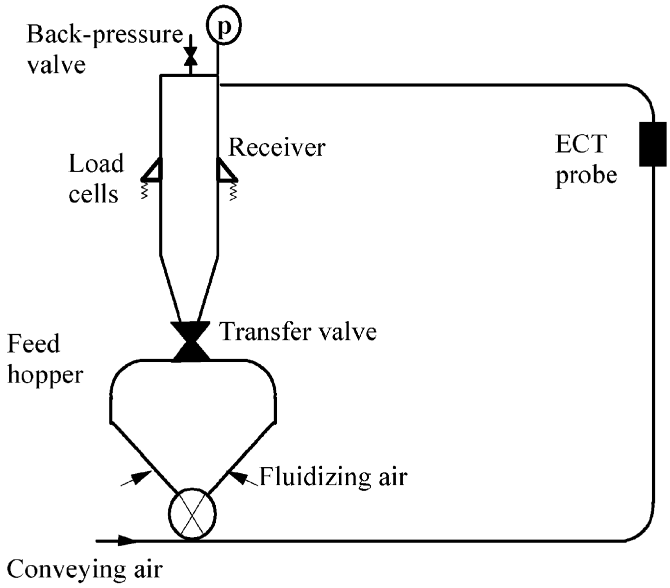

Fig. 2. Schematic of pneumatic conveying flow facility.

used to calculate the velocity across the cross-sectional area of the pipe. This allows an accurate measurement of the length and velocity of slugs in horizontal pipes, and can also be applied to dune flow and stratified flows. The ECT technique has been used successfully for monitoring dense phase flows and fluidisation properties, and its use is reported by Dyakowski et al. (1999), Jaworski and Dyakowski (2001), Zhu et al. (2003), Lee et al. (2004) and Fuchs et al. (2007) for dense phase conveying at low pressures. ECT measurements can provide information about what is present in the centre of the plugs of particles. Zhu et al. (2003) report what they call capsule flow. In this particles collect into rings around the pipe wall. These are not axially continuous but occur at regular intervals along the pipe travelling at about the gas velocity. Arko et al. (1999) and Hunt et al. (2003) have shown the methodology to give accurate measurements of solids flow rate the latter citing ±2%. However, that work was for millimetre sized particles.

This work is part of our applications of ECT to multiphase flow. Other examples are studies of gas/liquid flows, Baker et al. (2003), and liquid/liquid flows, Hasan and Azzopardi (2007). It complements our activities in metering of gas and solids flow rates in lean-phase conveying (Azzopardi et al., 1999; Giddings et al., 2006). This paper reports on the use of ECT to a pneumatic conveying industrial pilot plant and considers the fluctuations in flow that are observed, and their effect on the pulse and bulk mass flow rates.

2. Experimental facility

A pilot-scale facility, whose major features are shown schematically in Fig. 2, was used for the flow trials. The solids are fed through a rotary valve system operating at a range of speeds into the line where it is combined with the compressed air. It then passed along 8.7 m of horizontal pipe, round a 90° bend, up a 8.3 m vertical section around a second 90° bend and then along a 8.9 m horizontal section to the receiver vessel. This separates the air and solids. The former is discharged to atmosphere through a back-pressure valve whilst the solids are retained in the receiver for the duration of the test after which they are returned to the feed vessel by opening the transfer valve. The receiver vessel is mounted on load cells whose output is monitored continuously. Air flow is monitored by measuring the differential pressure across an orifice plate.

The material conveyed in this tests was coal originating from Thoresby colliery in Nottinghamshire. This had been ground to provide a fine powder. The size distribution, determined by sieve analysis, is shown in Fig. 3. The mass median diameter is 61 μm. The solids density was 1322 kg/m^3 and the (loose poured) bulk density was 537 kg/m^3. From this it was identified as a type A material according to the classification of Geldart (1973).

2.1. Measuring equipment

The probes used in these trials were manufactured at the University of Nottingham on a flexible printed circuit board (PCB). They consist of an array of eight electrodes 43 mm long with guard electrodes on either side of them. Two such arrays are mounted on a length of UPVC pipe with a Faraday cage around them. The centres of the electrode rings were 240 mm apart. The pipe inside diameter was 36.8 mm. The mask used to create the array is shown in Fig. 4. The probes were calibrated by taking readings with the pipe empty (gas only) and full of coal.

The results were obtained using a Tomoflow R100 ECT flow analysis system, comprising pipe-mounted sensor, data acquisition module, and control computer with real-time and off-line flow imaging and analysis software. A high-speed capacitance measurement unit with embedded PC as described by Byars

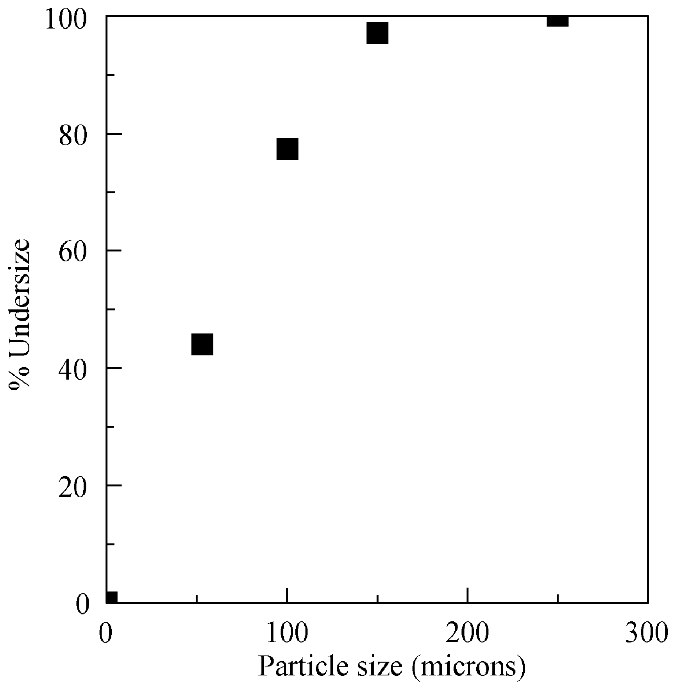

Fig. 3. Particle size distribution of conveyed material from sieve analysis.

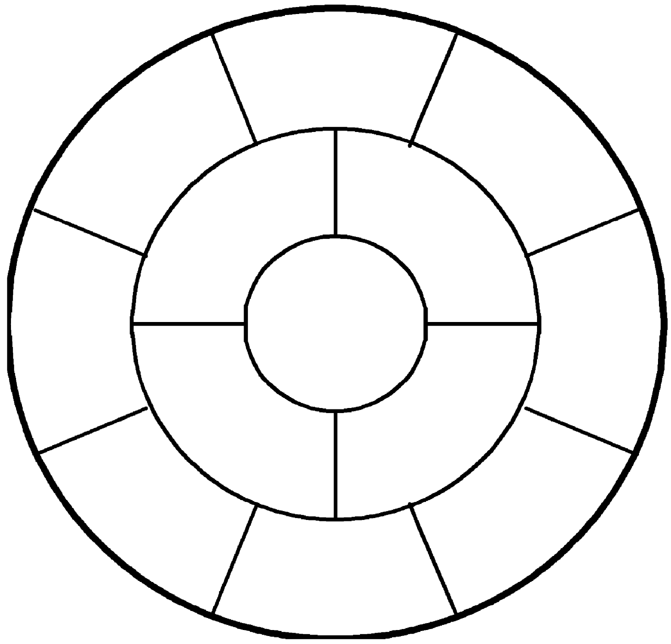

Fig. 5. Position of the 13 equal area zones employed—the eight external zones map onto the eight electrodes.

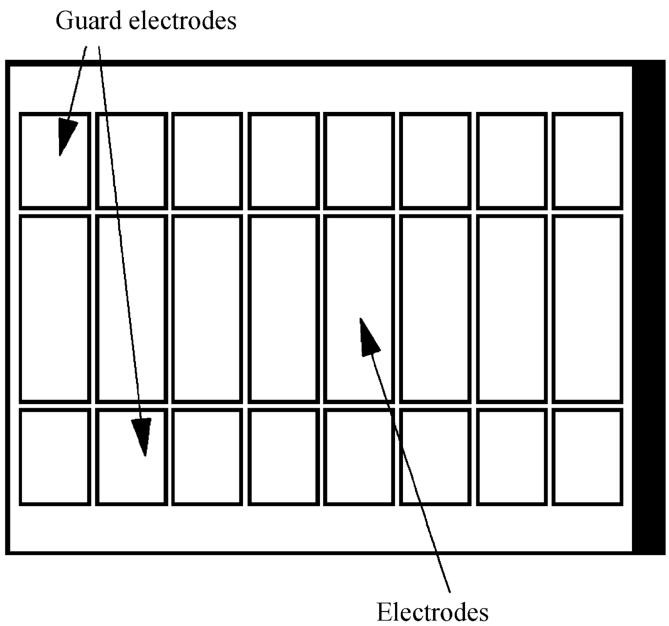

Fig. 4. Mask used to manufacture electrodes.

and Pendleton (2003) was employed. Twin-plane sensors with guard electrodes are utilised to create two, axially separated image 'planes' along the flow. Each 'plane' is, in fact, a cylinder of finite length made up of 812 pixels on a 32×32 square. Images of flows can be presented as circular maps with a grid of 32×32 pixels using a colour scale from black (pixel full of low permittivity material) to white (pixel full of high permittivity material). To investigate details of flow conditions it is more helpful to divide each image plane into a number of zones arranged appropriately for the flow conditions. For 8 electrode systems, dividing the flow into 13 zones containing approximately 62 pixels each and which have typical length scales of R axially and $R/2$ within the cross-section where R is the pipe radius. These zones are more consistent with the linear spatial resolution of ECT, which is sometimes quoted as $2R/n_e$ where n_e is the number of electrodes circumferentially around the pipe. Within each zone the pixel values are averaged to give one concentration value per zone for each frame of data. The positions of the 13 equal area zones used in the present work are shown in Fig. 5.

By correlating the instantaneous concentration of one plane with the same zone in the other plane the velocity at each point in time within each zone can be obtained. The result is plotted as a second graph with axes in cm/s on the right-hand side of the graph. The correlation process is described mathematically as:

$$R_{xy,i}(\tau) = \frac{\lim}{T \to \infty} \frac{1}{T} \int_0^T C_{1,i}(t) C_{2,i}(t+\tau)\, \mathrm{d}t, \qquad (1)$$

where $C_{1,i}(t)$ and $C_{2,i}(t)$ are the instantaneous concentrations in zone i in planes 1 and 2, respectively. Although mathematically the correlation is described for the averaging time T approaching infinity, in practice the velocity will fluctuate over some much shorter time scale and the user will need to set the window T at some suitable value appropriate to the particular length and velocity scales in the flow and the sensor geometry. If the flow structures are coherent over the sensor length, the resulting correlogram has a clearly discernible peak and contains information about the time domain statistics of the flow—primarily convection and dispersion. The simplest assumption is that the time delay at the peak of the correlogram corresponds to the transit time of flow structures between the two planes. The peak may be found by the greatest single value, centre of area or polynomial fitting. For these types of gravity particle-flows, a polynomial fitting is found to give the most consistent results though all the other techniques are available in the software. The time window used for the correlation process needs to be shaped in some way to minimise artefacts caused by sharp-edged windows. This shaping is known as apodization and various apodization functions are programmed into the software—the results use the common Hanning window, which is a smooth bell shape.

If $\tau_i(t)$ is the time delay at the correlogram peak for zone i at each frame at time t, then the transit is given by

$$V_i(t) = \frac{S}{\tau_i(t)}, \tag{2}$$

where S is the separation distance between the centre of the sensor electrodes. The volumetric flow per zone is given by

$$q_i = V_i(t) C_i(t) A_i \Delta t, \tag{3}$$

where Δt is the time interval between successive frames and A_i is cross-sectional area of each zone. $C_i(t)$ is in this case taken as the average of $C_{1,i}(t)$ and $C_{2,i}(t)$. The total volume flowing between time t_1 and t_2 can then be calculated as

$$Q = \sum_{t=t_1,t_2} \sum_{i=1,n} q_{i(t)}. \tag{4}$$

The concentrations $C_{1,i}(t)$ and $C_{2,i}(t)$ are instantaneous averages over a volume corresponding to $A_i \times L_s$, where L_s is the sensor electrode length. The velocity $V_i(t)$ is an average over a volume $A_i \times (L_s + S)$ and also a time average over the correlation window T. The volumetric flow rate, $q_i(t)$, is an average over the volume $A_i \times (L_s + S)$ and also a rolling average over T updated at each time frame t, q is often expressed in industrial situations as a 1 s value. The flow volume Q is integrated over the time period between time t_1 and t_2 and may be visualised as the equivalent to volume measurement through filling a tank over a time period.

ECT is inherently a fairly low resolution imaging system, but with very good overall accuracy on volume fraction estimation and thus on mass flow rate estimation in flows of distributed solids. The spatial resolution depends on the reconstruction algorithm used, but for the simple linear back-projection algorithm used here it is typically capable of resolving objects and edges with a 'smearing' of image across perhaps 5–10% of the pipe diameter. See Hunt et al. (2004) for typical images and resolution. On mass flow rate of solids the same paper demonstrates that accuracy of within 1% of reading is achievable when the solids are well characterised.

3. Results

In the study reported here, 10 runs were carried out. However, the following will focus on six of these. Table 1 provides some typical overall information about these runs.

The output from the load cell measurements was provided in the form of chart recorder traces. These were scanned and the data digitised. At the first level, time-averaged mass flow rates determined from the ECT results were compared with those from the load cell output. In the latter case the output was the variation in cumulative mass flow with time. Mass flow rate is obtained from the gradient. This approach has been applied to the outputs of run A. A time-averaged mass flow rate of 1.2775 kg/s was determined from the load cell data and a value of 1.284 kg/s from analysis of the ECT data. An accuracy of 0.5% was achieved; other runs gave agreement to within 1%.

Table 1
Flow rate used in runs

Run	Solids/gas mass flow ratio (kg/kg)	Solids mass flux (kg/m^2 s)
A	33	1209
B	24.7	1069
C	26	824–1081
D	26.7	1516
E	97.6	1468
F	48.8	1650
G	19	751

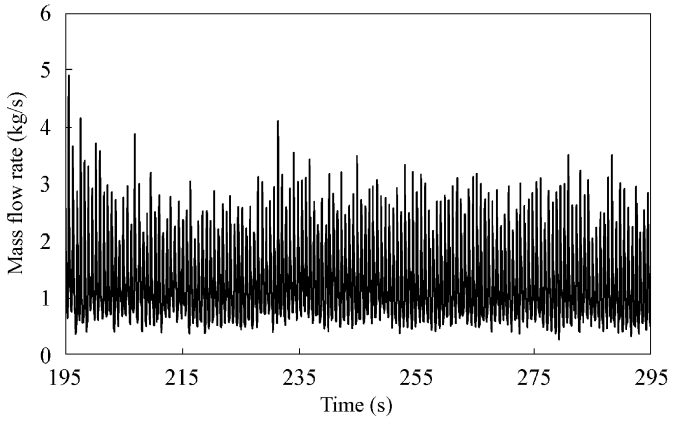

Fig. 6. Temporal variation of mass flow rate—run A—pressure = atmospheric.

Now, as the Tomoflow Electrical Capacitance Tomography software provides a great deal of detail of the solids flow passing the probe, its output was used to probe the flow further. Time-varying, cross-sectional distributions of concentration are available at intervals of 5 ms. The present investigation concentrates on the spatially averaged information which is in the form of a time-varying mass flow rate. In particular, we concentrate on a steady flow and on some with a long period ($\sim$ 10 s) fluctuations produced when the flow facility was tested to its limits.

Fig. 6 shows the temporal variation of mass flow rate for a steady run. The obvious, regular fluctuations are very visible if the time axis is expanded, Fig. 7.

In contrast, in some runs there were additional, longer-period fluctuations. The temporal variation of mass flow rate for run C is shown in Fig. 8 and an expanded view of part of the time sequence is presented in Fig. 9. These show that the original $\sim$ 1 Hz fluctuation is still there but that there is a second

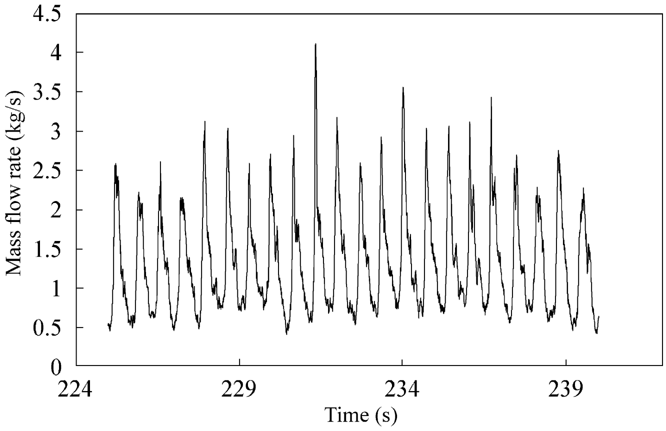

Fig. 7. Expanded version of part of Fig. 6.

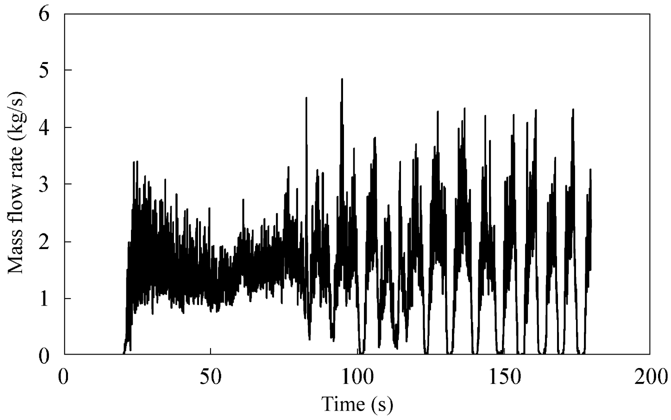

Fig. 10. Temporal variation of mass flow rate—run D—pressure=atmospheric.

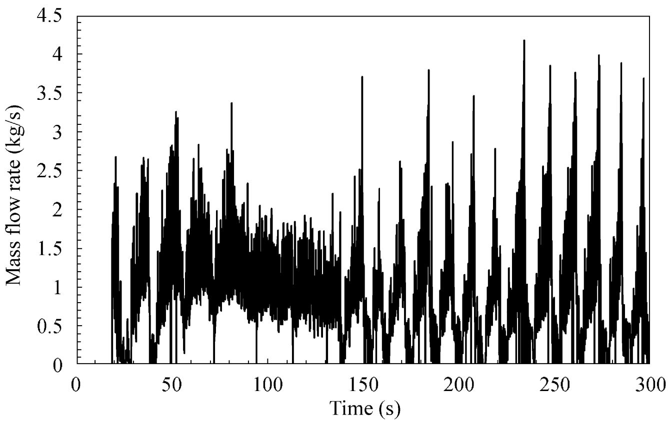

Fig. 8. Temporal variation of mass flow rate—run C—Pressure = 3 bar.

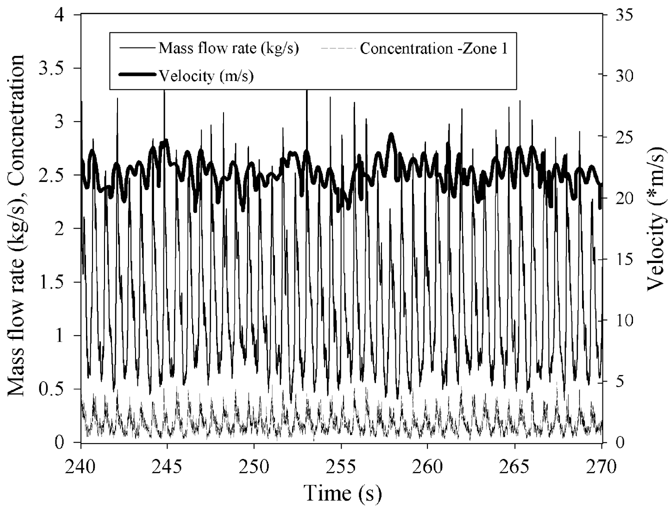

Fig. 11. Temporal variation of mass flow rate and concentration and velocity for zone 1—run A.

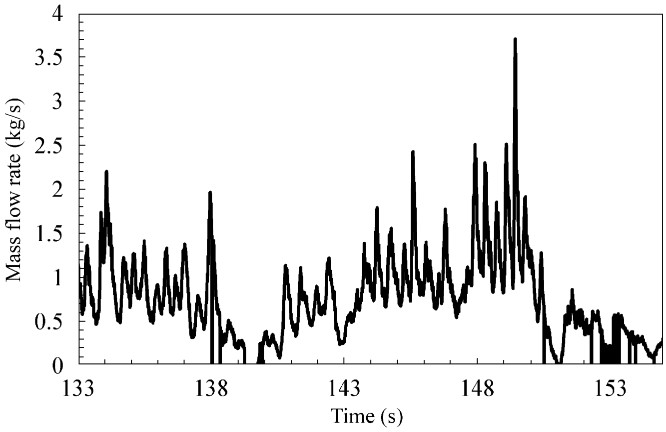

Fig. 9. Expanded version of part of Fig. 10.

longer-period fluctuation superimposed over this. Data from run D are illustrated in Fig. 10 and show that it is a repeatable phenomenon not a once off event. In these two runs the ECT data acquisition was started just before the powder feed was initiated so there is no data for an initial period.

In addition to mass flow rate, it is possible to extract concentration and velocity information. Typical results are shown in Figs. 11 and 12 where the concentration and velocities for one of the zones are shown together with the time-varying cross-sectionally averaged mass flow rate. These show that there are systematic fluctuations in velocity but these are a relatively small proportion of the mean value. However, like for the mass flow rate there are large fluctuations in concentration and the concentration fluctuates in step with the mass flow rate.

The comparison between the ECT output and that from the load cell is also excellent for those runs with the larger fluctuations. For these runs the cumulative mass flow rate from the load cells took the form of a wriggly line instead of the straight one for steady flows. As seen in Fig. 13 the ECT output follows the wriggles faithfully.

Examination of the cross-sectional distribution of solids concentration shows that the particles are concentrated around the pipe wall in axially regular pulses. There are hardly any particle in the centre of the pipe. It resembles the capsule flow described by Zhu et al. (2003). The capsules are the peaks of the fluctuations shown in Figs. 6–12. It is noted that the particle

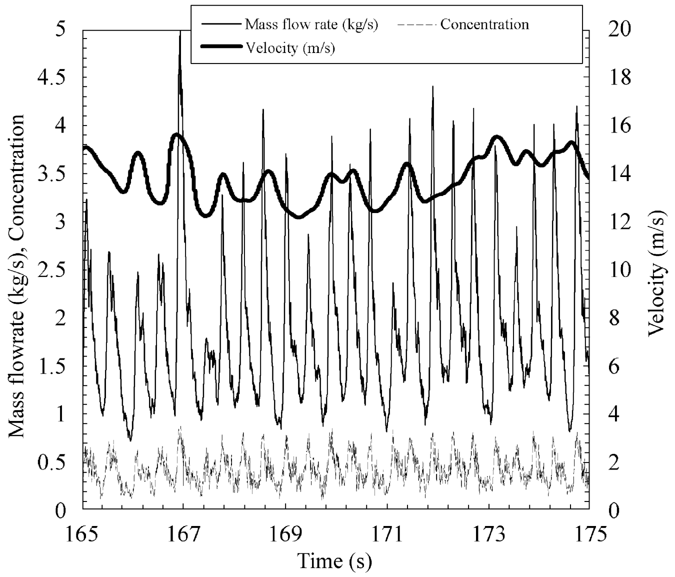

Fig. 12. Temporal variation of mass flow rate and concentration and velocity for zone 1—run E.

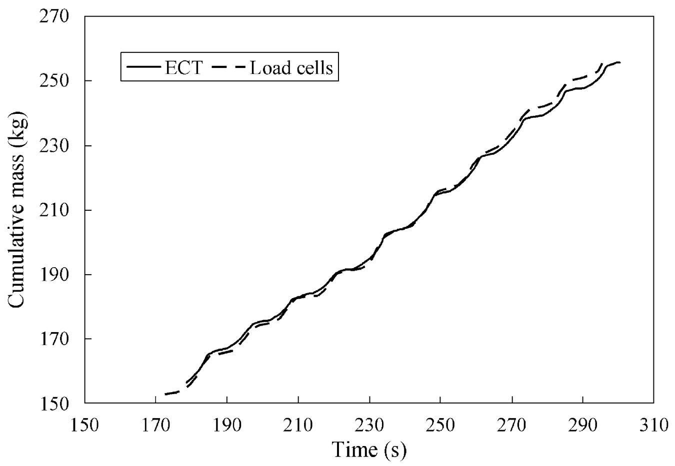

Fig. 13. Comparison of cumulative mass from load cells and ECT—run C.

sizes in the present work were much smaller than those used by Zhu et al. (2003) whilst the flow rates are much higher.

4. Discussion

Significant information can be gained from analysis of the mass flow rate time series information. The probability density function is a description of how often each value of mass flow rate occurs. The curve corresponding to run A is given in Fig. 14 and shows that the bulk of the data is distributed about a peak value with a longer tail towards higher flow rates, which represents the peak flow rates of varying magnitude.

The frequency characteristics of the systems can be obtained using power spectrum analysis. Here, power spectrum densities (PSDs) have been obtained by using the Fourier transform of

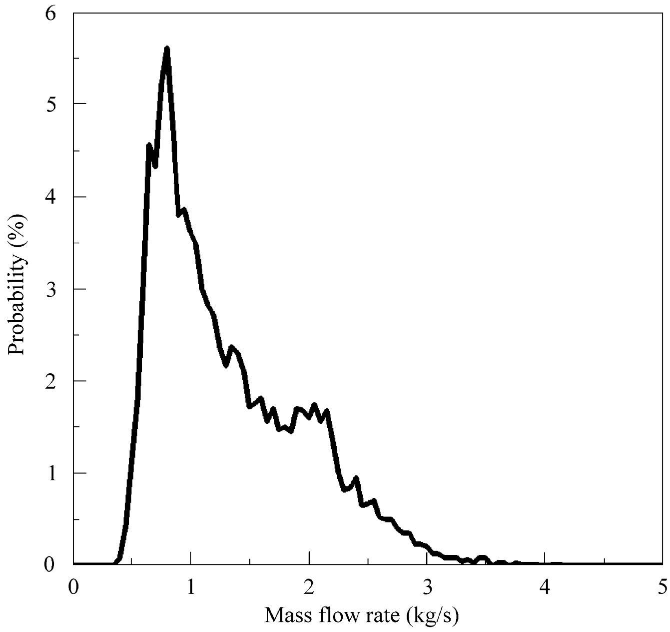

Fig. 14. Probability density function of mass flow rate—run A.

the autocovariance functions. Since the autocovariance function has no phase lag, a discrete cosine transform can be applied.

The autocovariance function of a signal $x(t)$ is given by

$$R_{xx}(k\Delta\tau) = \frac{1}{T-\tau}\int_0^{T-\tau} [x(t)-\bar{x}] \times [x(t+k\Delta\tau)-\bar{x}]\,\mathrm{d}t; \quad \tau < T, \tag{5}$$

where T is the sampling duration, $k\Delta\tau$ is the time delay, τ is the interrogating time delay and

$$\bar{x} = \frac{1}{T}\int_0^T x(t)\,\mathrm{d}t.$$

The PSD is then obtained from

$$P_{xx}(f) = \Delta\tau\left(\frac{1}{2}R_{xx}(0) + \sum_{k=1}^{\tau/\Delta\tau-1} R_{xx}(k\Delta\tau)w(k\Delta\tau)\cos(2\pi f k\Delta\tau)\right), \tag{6}$$

where $w(k\Delta\tau)$ is a windowing function. Windowing functions help to suppress the spectrum leakage which mostly comes out as the side lobes at the high frequency end of the spectrum. By using appropriate windowing function the frequencies contributing the system becomes clear.

In initial analysis carried out here, a basic cosine windowing function was used,

$$w(k\Delta\tau) = \cos\left(\frac{\pi k\Delta\tau}{2\cdot\tau}\right). \tag{7}$$

This analysis has been applied to the time series such as those shown in Figs. 6, 8 and 10 calculating autocorrelations and PSDs. The autocorrelations for four runs are shown in Fig. 15.

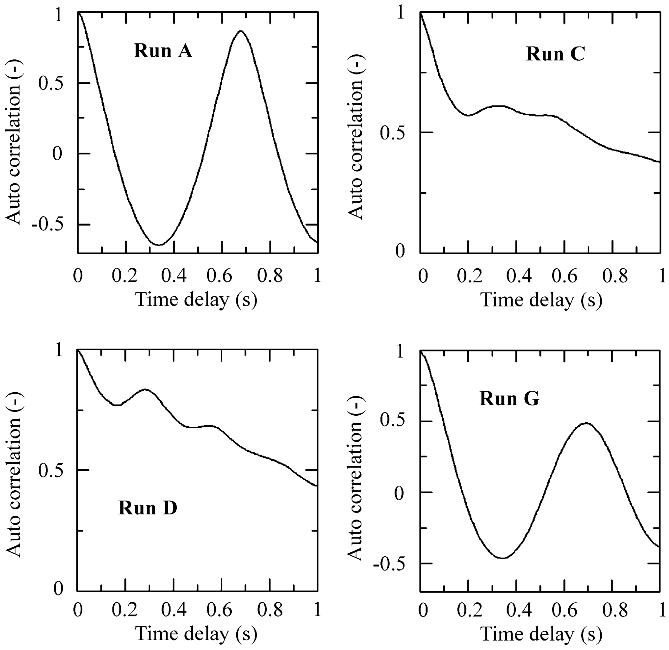

Fig. 15. Autocorrelations.

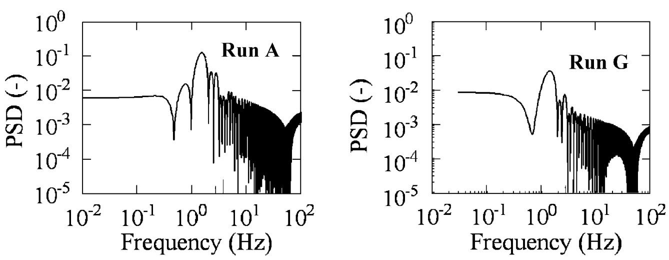

Fig. 16. Power spectral density—runs A and G.

The autocorrelations for runs A and G are fairly clear. As discussed by Groen (2004), by definition this function is equal to 1 at zero delay time. They then fall rapidly and oscillate around zero in a decaying sinusoidal curve. The first main peak can be associated with the mean interstructure time. The first zero crossing can be linked to the average structure passing time whilst the first minimum can be taken to indicate the maximum structure passing time. In contrast, the autocorrelations for runs C and D are much less clear being gradually decreasing with small dips. The power spectral densities show a single dominant peak for runs A and G (dominant frequency = 1.475, 1.425 Hz, respectively) as shown in Fig. 16. No clear peaks are observed for runs C and D. Yet as there were clear periodic structures in Figs. 8 and 10, the interrogation time delays were extended to see trends further into the autocorrelation (Fig. 17). In that figure, the autocorrelations show decaying sinusoidal curves similar to those for runs A and G shown in Fig. 17. The corresponding spectra exhibit not only a distinct peak at low frequency but a small peak at high frequency is obtained for both runs. This high frequency peak indicates that the small scale fluctuation is not as clear as the peak at low frequency

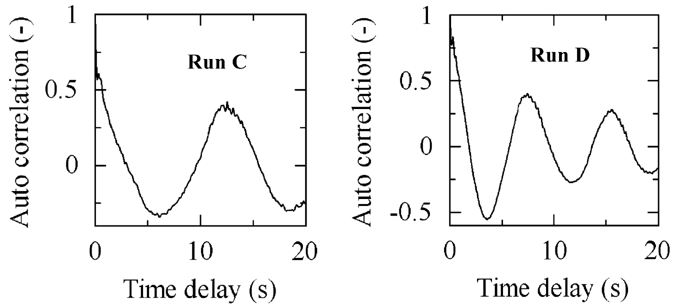

Fig. 17. Autocorrelations using longer interrogating duration for runs C and D.

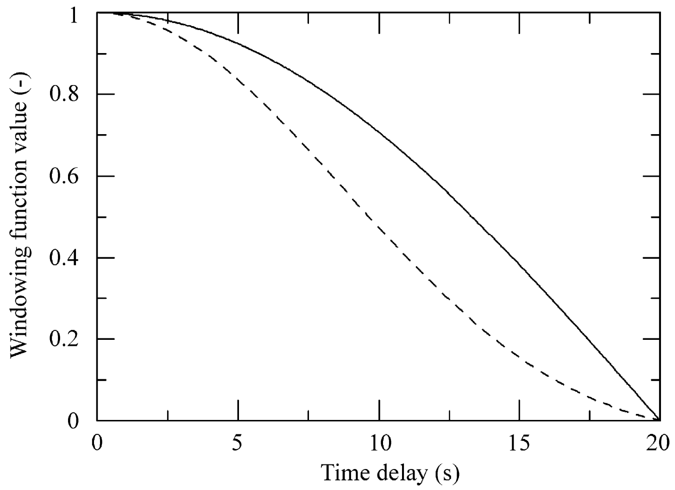

Fig. 18. Window functions (solid line: Eq. (7); dashed line, Eq. (8)).

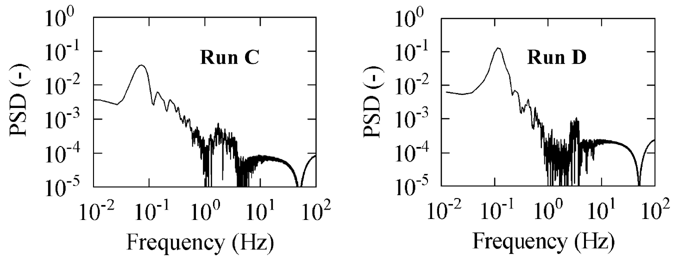

Fig. 19. Power spectral density—runs C and D.

probably due to spectrum leakage. To suppress the spectrum leakage further, an alternative windowing function proposed by Van Maanen (1999) having narrower width was applied:

$$w(k\Delta\tau) = \cos\left(\frac{\pi k\Delta\tau}{2\cdot\tau}\right)\cdot\exp\left[-0.5\left(\frac{k\Delta\tau}{p}\right)^2\right], \tag{8}$$

where p is a window factor which creates variety of width of window function. Increasing p produces a wider windowing function and $p = \infty$ reduces Eq. (8) to Eq. (7). In present study a value of $p = 2250$ was used. The two windowing functions are illustrated in Fig. 18. The final spectra for runs C and D are illustrated in Fig. 19.

Application of power spectral density analysis as outlined above permits the characteristic frequencies of these fluctuations to be determined. The peak frequencies determined from the plots for runs A and G are tied well with values obtained by counting the number of peaks over a given time. In the case of runs C and D, whose time series are shown in Figs. 8 and 10, the more extensive analysis, as discussed above, was employed. The power spectral densities of these runs displayed in Fig. 19 clearly show two peaks. The dominant frequencies are 0.0733, 1.73 Hz for run C and 0.1125, 3.425 Hz for run D. The lower frequency peak corresponds to the larger fluctuation whilst the higher frequency peaks characterise the second fluctuations superimposed on top.

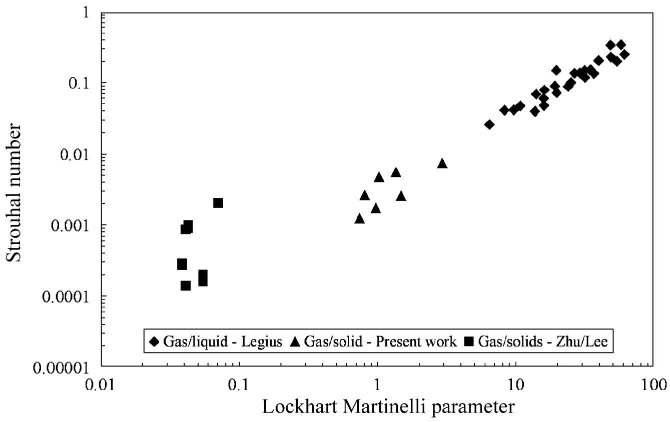

Fig. 20. Fluctuation frequency correlated as Strouhal number against Lockhart–Martinelli parameter.

A relationship was sought between the frequency and the flow parameters. Here, as in earlier work by Konrad and Davidson (1984), analogous behaviour in gas/liquid flow has been used to seek a means for correlating data. Azzopardi (2004) has drawn together data for the periodic structures in vertical gas/liquid flows and showed that the frequency of slugs of liquid could be related to the Lockhart–Martinelli parameter which is much used in pressure drop and heat transfer predictions. Fig. 20 shows a plot of Strouhal number (dimensionless frequency, $St = fD_t/u_{gs}$) versus the Lockhart–Martinelli parameter (which can be taken as the square root of the solids/gas momentum flux ratio, $M_R = \dot{m}_s^2/\rho_s\rho_g u_{gs}^2$). Also shown are the gas/liquid data of Legius et al. (1997) for slug flow in a vertical 50 mm diameter pipe. Though occurring at lower Strouhal numbers and Lockhart–Martinelli parameter that the gas/liquid data, the present data do show the same trend, all data lying on a line of slope 1. Also shown are data from gas/solids flow but from particles larger (3–4 mm) than those used in the present work. These were extracted from Zhu et al. (2003) and Lee et al. (2004). They also lie along the same line as the other data. From this, frequency is seen to depend on liquid or solids superficial velocity and there is little dependence on gas velocity.

As the solids are fed through a rotary valve system, there is a possibility of this being the cause of the above fluctuations. This is discounted because the frequencies deduced from the above analysis were significantly larger than the characteristic frequency of the feed device, e.g. feeder = 0.64 Hz, PSD = 1.47 Hz, manual counting of peaks = 1.47 Hz. Moreover, though there is some tendency for the structure frequency to increase with the setting of the feed device there is a significant

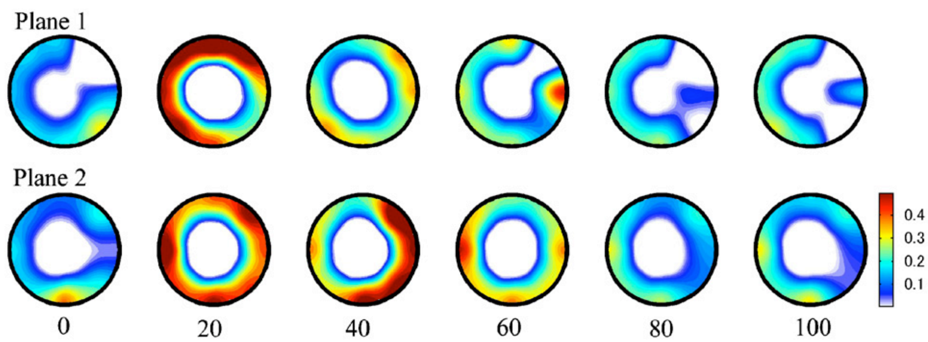

Fig. 21. Cross-sectional variation of solids concentration—run A. Figures indicate frame numbers which were taken at 200 Hz.

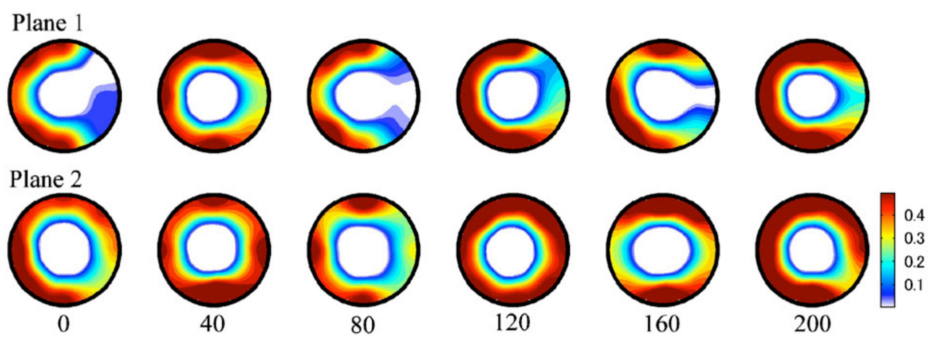

Fig. 22. Cross-sectional variation of solids concentration—run C. Figures indicate frame numbers which were taken at 200 Hz.

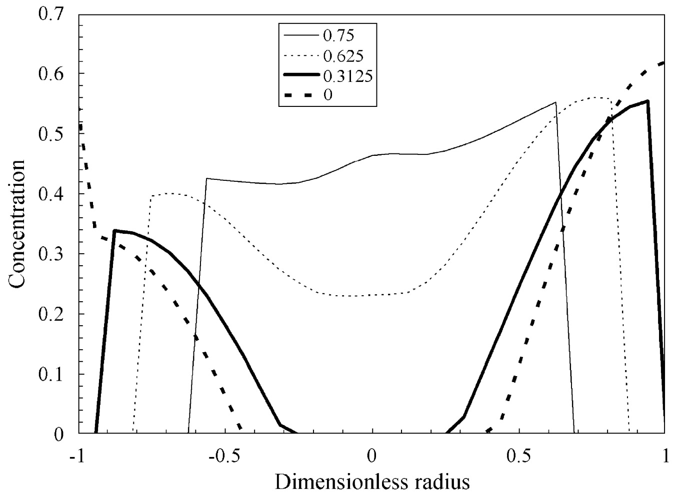

Fig. 23. Variation of solids concentration along chords at 0, 0.3125, 0.625, 0.75 pipe radii from centre–run C.

range of frequencies at the same setting. Additionally, the action of the 90° bend can be quite strong so the effect of inlet would probably not persist downstream. A number of papers, Jaworski and Dyakowski (2001), Zhu et al. (2003) and Lee et al. (2004), have reported these types of plugs of materials. They are a natural characteristic of the flow.

Examination of the ECT results in even further detail shows that the solids are flowing mainly along the walls. The extent to which solids penetrate towards the centre of the pipe increases during the peaks of and diminishes in the troughs of the high frequency pulses shown in Fig. 7, and are illustrated in Fig. 21. Each row shows images from one electrode plane selected at 0.1 s intervals and show the changes over one of the pulses. There is little difference between the images from the two electrode planes which is not surprising as the transit between planes corresponds to less than 10 frames. Data from run C, for which part of the time series is shown in Fig. 9, are displayed in Fig. 22. In this case the data are for time interval (0.2 s) between the frames. There are higher levels of concentration as expected from Fig. 9.

To appreciate the spatial variation of concentration the values along chords are shown for one frame in Fig. 23. Here the concentration is defined relative to the (loosely) packed bed state. The figure shows the relative rapid drop from the packed region to the empty region in the centre, i.e., the solids are found in the outer three quarters of the pipe cross-sectional area. The progression of this spatial variation of concentration with time can be followed in Fig. 24 which shows data across a diameter at time steps of 0.05 s. Each curve is transposed upwards by 0.1 to make viewing easier. It can be seen that the position of the higher concentration varies from side to side systematically. This aspect is picked out in Fig. 25 where the concentrations from positions close to the wall but at diametrically opposed positions are displayed. This information points to the pulses being fairly but not totally symmetrical. In some cases the right-hand side has the higher concentration first, in others it is the left-hand side. From this it is deduced

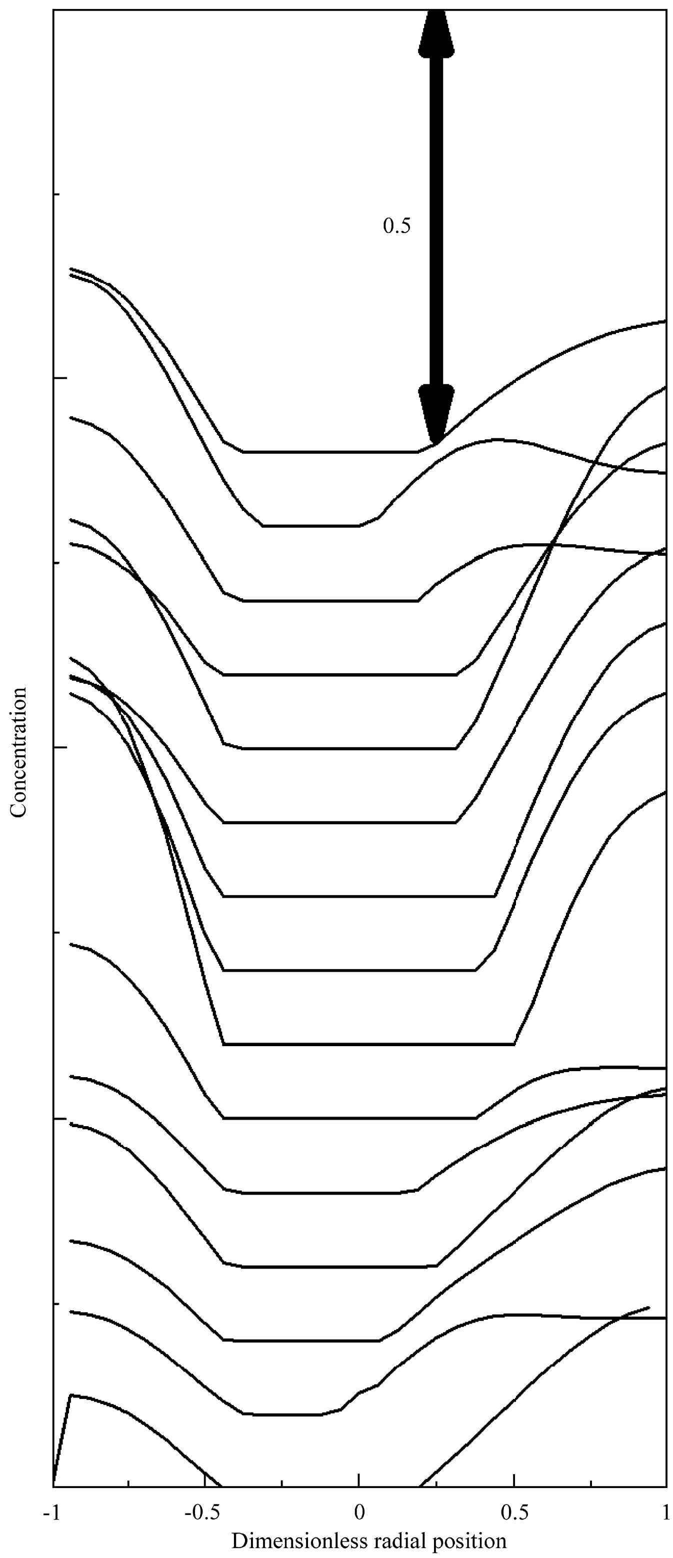

Fig. 24. Variation of concentration across a diameter—run A, different curves are from frames 50 ms apart. Curves are shifted up by 0.1 each time.

that there is not a strong component of swirl present as this would present one side always having the higher concentration first.

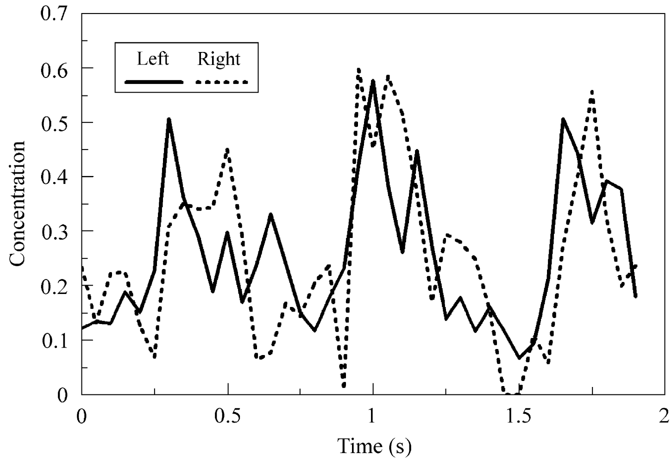

Fig. 25. Time variation of concentration on two different sides of the pipe—run A.

In contrast to the higher frequency fluctuations, the cause of the lower frequency pulses might be linked to effects at inlet. For those runs the pilot plant was being pushed to its limits. From the time series, the mass of solids in each of these large pulses was determined and found to be of the order of 10 kg. Based on this mass and the bulk density of the powder, a cube of side 26.5 cm is expected. This dimension is of the same size as the opening at the bottom of the feed hopper. This leads to the possibility that these pulses are the result of slip/stick flow at the hopper exit. By this it is implied that the powder forms an arch at the hopper exit which periodically collapses. The hopper does have a bottom cone of large angle. It also has aids to minimise sticking, e.g. fluidising air. However, these are positioned a short distance from the bottom. This might give a sufficiently large region to cause the slip/stick flow.

5. Conclusions

From the material presented above it can be concluded that:

1. Electrical capacitance tomography can give a very accurate measurement of the time-averaged solids mass flow rate for fine powders and supports earlier accuracy tests by Arko et al. (1999) and Hunt et al. (2003) for larger particles.
2. Two types of very periodic fluctuations were observed. The higher frequency one could be correlated to the phase flow rates and a relationship analogous to that for slug in gas/liquid flow looks very promising.
3. In some runs there was an additional fluctuation superimposed whose frequency was an order of magnitude smaller than the above. A suggested explanation for this pulsation is the occurrence of slip/stick at the feed point.

Notation

$C_{1,i}$	instantaneous concentrations in zone i, plane 1
$C_{2,i}$	instantaneous concentrations in zone i, plane 2
D_t	pipe internal diameter
f	frequency
L_s	sensor electrode length
$\dot{m}_s$	solids mass flux
p	window factor
P_{xx}	power spectral density
q_i	volumetric flow per zone
Q	total volume between t_1 and t_2
R_{xx}	autocovariance function
$R_{xy,i}$	correlation coefficient
S	separation distance between the centre of the sensor electrodes
T	sampling time
u_{gs}	gas superficial velocity
w	windowing function

Greek letters

Δt	time difference, s
ρ	density
τ	time delay at the correlogram peak for zone i, s
τ_i	interrogating time delay, s

Subscripts

G	gas
i	zone number
S	solids
1	lower plane
2	upper plane

Acknowledgements

The work reported here was part of a DTI funded project (#414) carried out by the University of Nottingham in partnership with Shaw Stone and Webster, Progressive Engineering Ltd. and Future Energy GmbH. The authors would like to thank Fred Anderton for his help in the construction of the probes.

References

Albright, C.W., Holden, J.H., Simons, H.P., Schmidt, L.D., 1951. Pressure drop in flow of dense coal–air mixtures. Industrial and Engineering Chemistry 43, 1837–1840.

Arko, A., Waterfall, R.C., Beck, M.S., Dyakowshi, T., Sutcliffe, P., Byars, M., 1999. Development of electrical capacitance tomography for solids mass flow measurement and control of pneumatic conveying systems. In: 1st World Congress on Industrial Process Tomography, Buxton, Greater Manchester.

Azzopardi, B.J., 2004. Bubbles, drops and waves: differences or underlying commonality. In: Invited lecture, 42nd European Two-Phase Flow Group Meeting, Genoa, 23–25 June.

Azzopardi, B.J., Teixiera, S.F.C.F., Pulford, C.I., 1999. A quasi-one-dimensional model for gas/solid flow in a venturi. Powder Technology 102, 281–288.

Baker, G., Azzopardi, B.J., Clark, W.W., Dyakowski, T., 2003. Transients in stratified/slug flow: observations using electrical capacitance tomography. In: BHRG Conference, San Remo.

Byars, M., Pendleton, J.D., 2003. A new high-speed control interface for an electric capacitance tomography system. In: 3rd World Congress on Industrial Process Tomography, Banff, Canada.

Dyakowski, T., Luke, S.P., Ostrowski, K.L., Williams, R.A., 1999. On-line monitoring of dense phase flow using real time dielectric imaging. Powder Technology 104, 287–295.

Fuchs, A., Zangl, H., Wypych, P., 2007. Signal modeling and algorithms for parameter estimation in pneumatic conveying. Powder Technology 173, 126–139.

Geldart, D., 1973. Types of gas fluidization. Powder Technology 7, 285–292.

Geldart, D., Ling, S.J., 1985. Dense phase conveying of fine coal at high total pressures. Powder Technology 62, 243–252.

Giddings, D., Azzopardi, B.J., Aroussi, A., Pickering, S.J., 2006. Absolute measurements of pneumatically conveyed powder using a single long throat venture. Powder Technology 172, 151–158.

Groen, J.S., 2004. Scales and structures in bubbly flows. Ph.D. Thesis, Technical University of Delft.

Hasan, N.M., Azzopardi, B.J., 2007. Imaging stratifying liquid–liquid flow by capacitance tomography. Flow Measurement and Instrumentation 18, 241–246.

Hunt, A., Pendleton, J., White, R.B., 2003. A novel tomographic flow analysis system. In: 3rd World Congress on Industrial Process Tomography, Banff, Canada.

Hunt, A., Pendleton, J., Byars, M., 2004. Non-intrusive measurement of volume and mass using electrical capacitance tomography. In: 7th Biennial ASME Conference on Engineering System Design and Analysis, 19–22 July, Manchester.

Jaworski, A.J., Dyakowski, T., 2001. Application of electrical capacitance tomography for measurement of gas–solids flow characteristics in a pneumatic conveying system. Measurement Science and Technology 12, 1109–1119.

Konrad, K., Davidson, J.F., 1984. The gas–liquid analogy in horizontal dense-phase pneumatic conveying. Powder Technology 39, 191–198.

Lee, L.Y., Quek, T.Y., Deng, R., Ray, M., Wang, C.-H., 2004. Pneumatic transport of granular materials through a 90° bend. Chemical Engineering Science 59, 4637–4651.

Legius, H.J.W.M., van den Akker, H.E.A., Narumo, T., 1997. Measurement on wave propagation and slug velocities in cocurrent upward two-phase flow. Experimental Thermal and Fluid Science 15, 267–278.

Matsumoto, S., Harakawa, H., 1987. Statistical analysis of the transition of the flow pattern in vertical pneumatic conveying. International Journal of Multiphase Flow 13, 123–129.

Van de Velden, M., Baeyens, J., Seville, J.P.K., Fan, X., 2007. The solids flow rate in the riser of a circulating fluidised bed (CFB) viewed by positron emission particle tracking (PEPT). Powder Technology, doi: 10.1016/j.powtec.2007.07.027.

Van Maanen, H.R.E., 1999. Retrieval of turbulence and turbulence properties from randomly sampled laser-anemometry data with noise. Ph.D. Thesis, Technical University of Delft.

Zhu, K., Rao, S.M., Wang, C.-H., Sandaresan, S., 2003. Electrical capacitance tomography measurements on vertical and inclined pneumatic conveying of solids. Chemical Engineering Science 58, 4225–4245.